

Two Growing Modes Lead to the Morphology-Quiescence Relation in Galaxies

Joanna Woo^{1*} & Sara L. Ellison¹

¹*Department of Physics & Astronomy, PO Box 1700 STN CSC, Victoria BC V8W 2Y2, Canada*

11 December 2021

ABSTRACT

Quiescence in galaxies correlates strongly with the central density/morphology of the stellar distribution. We investigate two possible explanations for this morphology-quiescence relation: 1) the central density results from a dissipative core-building event (“compaction”) that feeds an AGN that quenches the galaxy and 2) the central density results from inside-out growth by galaxy-wide star formation that is quenched by processes unrelated to the central density. We aim to distinguish these two scenarios using the MaNGA survey to determine profiles of stellar age, specific star formation rate (sSFR) and gas phase metallicity (O/H) as a function of stellar mass surface density within 1 kpc ($\Sigma_{*,1\text{kpc}}$) and total stellar mass (M_*). We find that gradients in age, sSFR and O/H depend on the galaxy’s position on the $\Sigma_{*,1\text{kpc}}-M_*$ diagram, suggesting two possible evolutionary pathways. The first pathway consists of galaxies with low $\Sigma_{*,1\text{kpc}}$ for their M_* whose centres are old, metal-rich and suppressed in sSFR compared to their outskirts, consistent with the inside-out growth scenario. The second pathway, consistent with the core-building scenario, consists of galaxies with higher $\Sigma_{*,1\text{kpc}}$ for their M_* , whose centres are younger, enhanced in sSFR and metal-deficient compared to their outskirts. Moreover, the WISE-selected AGN fraction peaks in the same area of the $\Sigma_{*,1\text{kpc}}-M_*$ diagram as the core-building pathway. The sSFR profiles of the quiescent population suggest that galaxies on the compaction-like path quench uniformly, while those on the inside-out growing path quench their centres first. Our results imply that both pathways contribute to the morphology-quiescence relation.

Key words: galaxies: general, galaxies: evolution, galaxies: structure, galaxies: stellar content

1 INTRODUCTION

It has been known for several decades that galaxies are divided into those that are star forming and those that are quiescent, and yet the physical causes for the cessation of star formation in galaxies (“quenching”) is still a matter of vigorous debate (e.g., Bell 2008; Peng et al. 2010, 2012; Woo et al. 2013; Omand et al. 2014; Woo et al. 2015; Zolotov et al. 2015; Lilly & Carollo 2016). An important observation is the strong correlation between quiescence and bulge-like morphology or high central density. Quiescence, as quantified by colour or the star formation rate (SFR), correlates strongly with visual morphological classification (Strateva et al. 2001; Schawinski et al. 2014), the bulge-to-total ratio or the bulge mass (Bluck et al. 2014; Teimoorinia et al. 2016), concentration (Strateva et al. 2001; Kauffmann et al. 2004), the Sersic index (Bell 2008; Wuyts et al. 2011; van

Dokkum et al. 2011; Mendel et al. 2013), line-of-sight velocity dispersion (van Dokkum et al. 2011; Teimoorinia et al. 2016; Bluck et al. 2016), the surface density within an effective radius (Kauffmann et al. 2004; Omand et al. 2014), and the surface density within a 1 kpc (Cheung et al. 2012; Fang et al. 2013; Woo et al. 2015, 2017). Furthermore, these correlations are stronger than the correlations between quiescence and other properties such as total stellar mass and the environment (Bluck et al. 2014; Woo et al. 2015; Teimoorinia et al. 2016).

Although not all of the above quantities are strictly “morphology”, they are closely related. For example, the line-of-sight velocity dispersion is a measure of the random motions typical of stars in a bulge rather than the ordered motions of disks. The high Sersic index of bulges indicates a strongly peaked density of stars in the centres, or a high central surface density (within 1 kpc or effective radius). Thus, we refer to the above observations collectively as the “morphology-quiescence relation”.

* joannawoo@uvic.ca

The morphology-quiescence relation has led many to argue for a causal relationship between the building of the core/bulge of a galaxy and its eventual quenching (Bell et al. 2012; Bluck et al. 2014). Heating by an active galactic nucleus (AGN) has been a particularly compelling hypothesis. In this picture, dissipative inflows of gas triggered by mergers (Barnes & Hernquist 1991; Mihos & Hernquist 1996; Hopkins et al. 2006; Zolotov et al. 2015) or disk instabilities (Friedli & Benz 1995; Immeli et al. 2004; Bournaud et al. 2011) feed a central starburst which builds the density of a galaxy’s inner core (a process called “compaction” in the literature since it results in more compact galaxies - Zolotov et al. 2015). The same inflows feed an AGN which heats and/or expels cold gas from the system preventing further star formation.

In support of the AGN hypothesis, the directly measured masses of supermassive black holes are tightly correlated with bulge velocity dispersion (Kormendy & Ho 2013) as well as the specific star formation rate (sSFR; Terrazas et al. 2016, 2017). Furthermore, the fraction of X-ray detected AGN at high- z peaks for galaxies with high sSFR and high core densities (Kocevski et al. 2017). In addition, some tentative evidence that AGN can expel significant amounts of gas from a system has been observed in the local universe (Cheung et al. 2016; Baron et al. 2018; Bradford et al. 2018; but see also Ho et al. 2008; Fluetsch et al. 2018; Shangguan et al. 2018 for a contrary view).

Despite widespread support for the compaction hypothesis, others, notably Lilly & Carollo (2016), argue that the morphology-quiescence relation can be reproduced by a simple model of disk growth that requires no special bulge formation events at all. These authors propose growing galaxies by successively adding exponential disks of star-forming gas whose scale lengths grow with the expansion of universe (see also Nelson et al. 2012, 2013). Disks grown in such an “inside-out” manner result in apparently older centres and younger outskirts. In fact, such inside-out disk growth is expected as a natural consequence of the expansion and turn-around of shells of dark matter in the top-hat spherical collapse model, where the innermost shells, which collapse first, have the lowest angular momentum (Kepner 1999; see also Fall & Efstathiou 1980; van den Bosch 1998, 2002). Hydrodynamical simulations (e.g., Roškar et al. 2008) have confirmed that galaxies growing in isolation grow inside-out, producing negative age gradients (older centres, younger outskirts).

Lilly & Carollo (2016) applied a quenching model to their inside-out growing galaxies such that the quenching probability depended only on its stellar mass M_* , i.e., more massive galaxies are more likely to be quenched. They did not specify the physical nature of the quenching mechanism, but note that M_* is a proxy for the halo mass for isolated galaxies which may play a role in quenching (Dekel & Birnboim 2006; Woo et al. 2013, 2015). Using their simple model, Lilly & Carollo (2016) demonstrated that the morphology-quiescence relation derives simply from the fact that more massive galaxies reach a high enough quenching probability earlier than less massive galaxies. When a galaxy quenches earlier, its scale length is smaller and it appears structurally denser. (This effect is an example of the “progenitor bias” pointed out by van Dokkum & Franx 2001).

The processes of secular disk building plus early quench-

ing and dissipative bulge/core-building (“compaction”) therefore represent two entirely different mechanisms that have been proposed to explain the observed morphology-quiescence relation in galaxies. The observation that denser quiescent galaxies are older than less dense galaxies has been interpreted as evidence of progenitor bias (Tacchella et al. 2017). However, this by itself does not rule out compaction-like scenarios for building old bulges since the more violent forms of disk instability are predicted to occur at high redshift ($z \sim 2$), at the peak of the cosmic star-formation history and global accretion rate history (Kereš et al. 2009; Zolotov et al. 2015).

Distinguishing between core-building compaction-like scenarios and progenitor effects of inside-out growth depends crucially on the presence or lack of new star formation in the centres of galaxies. If galaxies are growing by secular inside-out disk growth by default, then the newest stars are found in the disk. A compaction event on the other hand, *adds* new stars to the centres of otherwise inside-out growing disks. Thus the signature of secular disk growth is a negative age gradient while the signature of a compaction-like event is a more positive (less negative) age gradient.

With the recent advent of large integral field unit (IFU) surveys of nearby galaxies such as MaNGA (Mapping Nearby Galaxies at the Apache Point Observatory - Bundy et al. 2015), CALIFA (Calar Alto Legacy Integral Field spectroscopy Area - Sanchez et al. 2012) and SAMI (Sydney-AAO Multi-object Integral field spectrograph - Croom et al. 2012), we can begin to study the age gradients of galaxies as a function of global properties, which is the subject of this paper. Indeed some papers have already presented stellar population gradients in CALIFA disks (Sánchez-Blázquez et al. 2014) and in the general population in MaNGA (Godard et al. 2017), finding various trends of the age gradient with global properties. What is missing is a comprehensive synthesis of what these age gradient trends mean in the context of our current understanding of structural growth and quenching.

Our goal is to explore whether compaction-like core-building events contribute to the build-up of the central density of galaxies and whether this is related to quenching. Thus, this paper is a study of the gradients and profiles of stellar age, sSFR and gas phase metallicity as a function of the central density and M_* .

2 DATA

2.1 Sample

Our sample is drawn from the MaNGA survey (Bundy et al. 2015). The current release at the time of writing (Data Release 14 or DR14) includes 2780 galaxies. The MaNGA targets were drawn from the NASA-Sloan Atlas (NSA) catalogue (Blanton et al. 2011). In order to obtain global properties for each MaNGA object, each MaNGA target was matched to the Sloan Digital Sky Survey (SDSS) DR7 spectroscopic catalogue, requiring a match separation of $< 3''$. This produced 2674 matches with a unique SDSS objID.

We draw upon various public catalogues of global properties with inhomogeneous sample definitions, including catalogues of global star formation rate (Brinchmann et al.

2004), group membership (Yang et al. 2012), disc inclination measurements (Simard et al. 2011), and products from the DR7 photometric pipeline (see the following subsections for details). We have found that 1904 MaNGA objects appear in every catalogue that we use.

The questions posed in this study concern the quenching and morphological evolution of *isolated* galaxies since galaxies in groups and clusters are expected to experience additional quenching mechanisms due to their environment (Gunn & Gott, J. Richard 1972; Larson et al. 1980; Read et al. 2006; Villalobos et al. 2012; Woo et al. 2015, 2017). The morphological evolution of group/cluster galaxies will be addressed in future work. In our present study, we restrict our sample to those galaxies that belong in Yang et al. groups with only 1 member. We call these “isolated” galaxies. This reduces the sample to 1008 galaxies.

In order to parameterize the central density, we use the stellar surface density within 1 kpc ($\Sigma_{*,1\text{kpc}}$). The primary reason for this choice is that $\Sigma_{*,1\text{kpc}}$ is a measure of what happens to the core (inner kpc), whereas a scale radius (eg. a half-light or half-mass radius) also responds to events happening in the outskirts. The actual scale of 1 kpc (as opposed to 2 or 0.5 kpc) was chosen as a seeing-constrained measure of the core in the nearby universe and likely does not correspond to anything physical. The details of our $\Sigma_{*,1\text{kpc}}$ measurement are given in §2.2.

Due to the seeing of the SDSS, we restrict our sample to those galaxies with $z < 0.07$, and we also require that the point spread function (PSF) width in the r -band be less than 1 kpc in radius. Since MaNGA targets were selected to be nearby, these cuts removed only 62 objects. By far the most aggressive cut (after the isolation criterion) was our cut in disc inclination (from the catalogue of Simard et al. 2011) $b/a > 0.4$ meant to minimize significant errors due to dust. After this cut, the sample size is 639. We also required the total masses to be $M_* > 10^9 M_\odot$, yielding 596 galaxies.

Lastly, we applied various quality control cuts to the age, sSFR and gas phase metallicity measurements in the MaNGA cubes (see below) which further reduced the sample to 581 galaxies for studying stellar properties (namely age), and 500 galaxies when studying gas properties (sSFR and O/H).

In all the following calculations we have assumed the following cosmology: $\Omega_m = 0.3$, $\Omega_\Lambda = 0.7$ and $h = 0.7$.

2.2 Global Quantities

We computed the surface density of stars within 1 kpc $\Sigma_{*,1\text{kpc}}$ by fitting the synthetic spectral energy distributions (SEDs) to the SDSS DR7 surface brightness profiles of each galaxy. This is an improved version of the computation in Woo et al. 2015 where the SED fitting was performed by the KCORRECT code of Blanton & Roweis 2007. The M/L ratios of the latter code are known to be underestimated for red SEDs - Blanton & Roweis 2007.

The synthetic SEDs were constructed using the PEGASE 2 stellar population synthesis code of Fioc & Rocca-Volmerange (1999) and the BaSeL stellar library (Lejeune et al. 1998). We assumed a Kroupa initial mass function (IMF) spanning 0.1-120 M_\odot , the type-II supernova (SNII) ejecta model B of Woosley & Weaver (1995), and enabled stellar winds. We constructed 72 simple stellar population

(SSP) models that obeyed “ τ -models” of star formation histories of the form:

$$\dot{M}_*(t) \propto t/\tau e^{-t/\tau} \quad (1)$$

The τ -models spanned a range of 9 initial metallicities ($Z = [0.0001, 0.0004, 0.004, 0.008, 0.01, 0.02, 0.03, 0.05, 0.1]$) and 8 values of τ ($\tau = [0.1, 0.5, 1, 1.5, 2, 2.5, 3, 4]$ Gyr), and were sampled at 20 time steps from 50 Myr to 13 Gyr, yielding 1440 synthetic SEDs. The PEGASE code evolves the metallicity of the population self-consistently such that the stars formed in the next time step adopt the metallicity of the ISM which was enriched by the stars in the previous time step. The code also adds light from nebular emission (see Fioc & Rocca-Volmerange 1999). The resulting synthetic spectra were convolved with the SDSS *ugriz* filters in order to produce *ugriz* SEDs. For each radial bin in the *ugriz* surface brightness profile of each galaxy, we find the best-fitting synthetic SED and adopt the predicted M/L_r of the population and age to estimate the stellar mass within the profile bin. (In keeping with standard practice in the literature, this mass includes remnants, but not the mass returned to the interstellar medium - ISM). In this way, we were able to construct stellar mass profiles which were converted into cumulative mass profiles. We then interpolated the profiles to find the mass within 1 kpc.

In the same way, we computed total stellar masses M_* by fitting synthetic SEDs to the extinction-corrected *ugriz* total Petrosian magnitudes from SDSS DR7, which were k -corrected to $z = 0$ using the code of Blanton & Roweis (2007). We then interpolated the cumulative mass profiles to find the radius that contains half the total mass ($R_{e,\text{mass}}$) that was computed from the total Petrosian magnitudes. We performed our own measurement of M_* in order to determine $R_{e,\text{mass}}$ self-consistently with the cumulative mass profiles. However, in order to be more easily compared to other work, for our $\Sigma_{*,1\text{kpc}}-M_*$ diagrams, we adopted the M_* values from the widely used MPA-JHU DR7 catalogue¹ (Kauffmann et al. 2003; Salim et al. 2007), which also use the Kroupa IMF. However our results are not sensitive to the choice of M_* measure.

Total star formation rates are from the DR7 extension of the those computed by Brinchmann et al. (2004) which are also from the MPA-JHU catalogue¹.

2.3 MaNGA Stellar Ages

We downloaded the publically available data cubes from the DR14 data release of MaNGA² as well as the summary table for the MaNGA Data Reduction Pipeline³ which includes redshifts from the NSA catalogue (Blanton et al. 2011). There are 2780 galaxies (and 2044 stars) in this sample (which will be reduced after matching with DR7 - §2.1 - see below). For each galaxy, we computed the signal-to-noise ratio in each spaxel (S/N) averaged over the observed wavelength range that corresponded within the rest-frame range of 5590-5680 Å, which is a range that is relatively

¹ <https://wwwmpa.mpa-garching.mpg.de/SDSS/DR7/index.html>

² <https://www.sdss.org/dr14/manga/manga-data/data-access/>

³ <https://data.sdss.org/sas/dr14/manga/spectro/redux/v2.1.2/drpall-v2.1.2.fits>

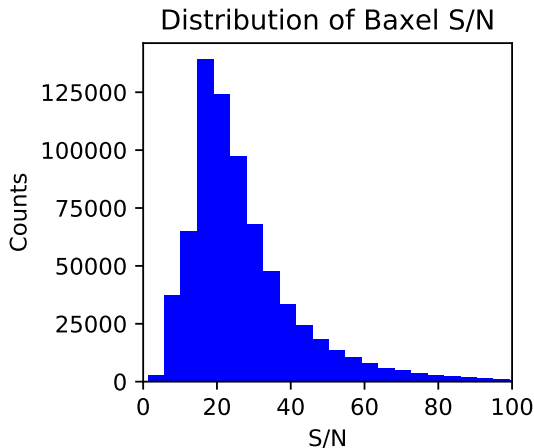


Figure 1. The distribution of S/N averaged over the rest-frame wavelength range of 5590-5680 Å for all baxels.

devoid of emission lines and sky lines. After masking out foreground stars as well as spaxels with $S/N < 2$, we used the Voronoi binning method of Cappellari & Copin (2003) to adaptively bin remaining adjacent spaxels such that their resulting S/N reaches our target value (determined below). We refer to these Voronoi bins of spaxels as “baxels”.

To account for the covariance of the noise between adjacent spaxels, we multiply the quadrature-added noise of the binned spaxels by the correction factor computed by Law et al. (2016): $1.0 + 1.62 \log(n)$, where n is the number of binned spaxels when $n < 100$. For $n \geq 100$, the correction factor is a constant 4.2. For some galaxies, the total S/N of the entire cube is such that a target S/N of 20 per baxel cannot be reached and the algorithm fails. Thus instead of a fixed target S/N, we use either 20 or the maximum S/N of all spaxels, whichever is lower, when Voronoi binning. We save the target S/N as well as the actual S/N of each baxel in order to use it in our error analysis below. 231 out of 2780 galaxies were binned to a target S/N less than 15. Applying this binning to the whole MaNGA sample of 2780 galaxies resulted in 716064 baxels. The distribution of S/N for all baxels is shown in Fig. 1.

Each baxel is corrected for foreground Galactic extinction using the extinction curve of Fitzpatrick (1999).

We performed full spectral fitting on each baxel using the Penalized Pixel Fitting (pPXF) algorithm of Cappellari (2017) (which is an upgrade of the original algorithm presented in Cappellari & Emsellem 2004). The SSP models that are fitted to the baxels are the E-MILES templates produced by Vazdekis et al. (2012); Ricciardelli et al. (2012); Vazdekis et al. (2016) using the Kroupa (2001) IMF and BaSTI theoretical isochrones (Pietrinferni et al. 2004). Since our fitting wavelength range includes 7385-8950 Å which covers the CaII triplet, we limit the grid of SSP models to those in the “SAFE” ranges⁴ of metallicity (7 grid points $-0.66 < [M/H] < 0.4$) and age (52 grid points for 0.03-13.5 Gyr) for using this wavelength range. Since our final sam-

ple consists of low- z (< 0.07) massive ($> 10^9 M_\odot$) objects (see §2.1) we do not expect real metallicities to fall outside of this safe range⁵. This produces an age-metallicity grid of 364 templates.

The pPXF algorithm computes the weights that produce the best-fitting linear combination of the templates that reproduces the observed spectrum. It fits emission lines simultaneously such that the stellar population of star forming galaxies can be fitted despite emission filling in important absorption lines. We have included the Balmer lines down to H δ , HeI, [SIII], [ArIII], and the doublets of [OII], [SII], [OIII], [OI] and [NII]. Forbidden lines are fixed to share a common, single, velocity component. The Balmer lines are also fixed to a common velocity, but the Balmer velocity component is allowed to be distinct from the velocity component of the forbidden lines. We use the weights computed by pPXF to estimate the mean mass-weighted log age and metallicities for each baxel.

pPXF includes the option to regularize the solution such that the weights represent a more physical, smooth star formation history and chemical enrichment evolution. Our tests have indicated that the accuracy of the mean mass-weighted log age and metallicities for the regularized solutions is similar to the non-regularized version. Since the computation time for full regularization is more than 10 times longer than the non-regularized solution, we have opted to compute the non-regularized solutions for this study.

We tested the accuracy of stellar ages and metallicities computed by pPXF by fitting simulated spectra with known ages and metallicities, and with the same wavelength range, resolution and noise typical of our baxels. We found that in 97% of the cases, both the ages and metallicities are recovered with less than 0.2 dex scatter. We found very minimal offsets of less than 0.1 dex. Full details of our tests are presented in the Appendix.

From our tests, baxels had “good” ages if they fulfilled the following criteria:

- (i) the χ^2 of the fit < 5 (99% of our baxels)
- (ii) S/N of the baxel > 10 (87% of our baxels)
- (iii) $E(B-V)_{\text{stars}} < 0.28$ (computed from the shape of the continuum, specifically the multiplicative polynomial outputted from pPXF) (95% of our baxels)
- (iv) the output mass-weighted log age/yr was greater than 8.5 (~ 300 Myr) (99.7 % of our baxels)
- (v) they contain < 10 spaxels (92% of our baxels)
- (vi) they have > 2500 valid wavelength pixels (non NaNs) (99.6% of our baxels)

where the first four criteria were motivated by our tests in the Appendix. Out of the 2780 MaNGA objects, these cuts resulted in a total of 564355 baxels in 2641 galaxies. After matching with the SDSS DR7 catalogues and applying the cuts in §2.1, we are left with 108997 baxels in 581 galaxies. This is the sample of baxels used when studying stellar age gradients and profiles.

⁴ <http://www.iac.es/proyecto/miles/pages/ssp-models/safe-ranges.php>

⁵ We also performed the analysis using the more standard range of 3500-7429.4 Å, included metallicities down to $[M/H] = -1.2$, and found that our results do not change significantly.

2.4 Surface Densities of Stellar Mass, Star Formation Rates and Gas Metallicities

The stellar mass surface density (Σ_*) in each baxel is computed from the r -band luminosity density of the observed spectrum and the combined mass-to-light ratio in the r -band obtained by applying the pPXF weights to the mass and light of the individual templates (assuming the Kroupa 2001 IMF).

pPXF simultaneously fits the flux (density) and velocity of the emission lines with the stellar populations. We use these flux measurements for the baxels instead of for individual spaxels to compute SFR and gas metallicity. The voronoi binning allows for more accurate subtraction of the stellar contribution, and accounts for the correlated errors between adjacent spaxels when computing S/N for the lines.

We computed the gas reddening from the Balmer decrement and dust-corrected the fluxes for all lines. We then computed the SFR from the corrected $H\alpha$ luminosities using the expression given in Kennicutt et al. (2009): $\text{SFR}(M_\odot \text{yr}^{-1}) = 5.5 \times 10^{-42} L_{H\alpha}(\text{ergs}^{-1})$, which is valid for electron temperatures of 10^4 K and Case B recombination (the gas processes all ionizing photons), and assumes the Kroupa (2001) IMF. Since the fluxes are measurements of flux density, this is an estimate of SFR density (Σ_{SFR}). The specific star formation rate for each baxel (sSFR) is then $\Sigma_{\text{SFR}}/\Sigma_*$.

Gas-phase metallicities are computed using the Marino et al. (2013) calibration: $12 + \log(\text{O}/\text{H}) = 8.533 - 0.214(y - x)$, where $y = \log[\text{O III}]/H\beta$ and $x = \log[\text{N II}]/H\alpha$. (We often abbreviate $12 + \log(\text{O}/\text{H})$ as “O/H”).

When studying the profiles of sSFR and O/H, we applied the following cuts to baxels:

- (i) cuts (v) and (vi) listed in §2.3 (the emission line fitting tends to be robust against errors in the stellar population fitting, so we do not apply the other criteria);
- (ii) the criterion for ionization from star-formation (no composites): $y < 0.61/(x - 0.05) + 1.3$ (Kewley et al. 2006), where $y = \log[\text{O III}]/H\beta$ and $x = \log[\text{N II}]/H\alpha$;
- (iii) the $\text{S/N} > 3$ for the four emission lines used in (ii);
- (iv) $\text{E}(\text{B}-\text{V}) < 1.3$ from the Balmer decrement (only one galaxy had baxels with extremely high $\text{E}(\text{B}-\text{V})$).

All the above cuts left us with 277326 baxels with gas inside 2075 galaxies. After matching with the SDSS DR7 catalogues and applying the cuts in §2.1, we have 72749 baxels in 500 galaxies. This is the sample of baxels used in the analysis of gas profiles and gradients (i.e., of sSFR and gas metallicity).

2.5 Gradients and Relative Offsets in Age, sSFR and O/H

Gradients of stellar age, sSFR and gas metallicity for each galaxy were computed as the slope of the linear fit of the quantity of interest vs the galactocentric distance of the baxels (from the centres measured in the NSA catalogue - Blanton et al. 2011) in units of the half-mass radius $R_{e,*}$. A gradient was only computed if there were at least 10 good baxels (as determined by the criteria in §2.3 and 2.4). Only 4 objects did not fulfill this criterion when computing the age

gradients, while 75 objects had fewer than 10 good baxels for measuring sSFR and O/H gradients.

In order to compare relative enhancements and deficits in stellar age, sSFR and O/H between baxels in different galaxy samples, we computed offsets in these quantities $\Delta \log \text{age}$, $\Delta \log \text{sSFR}$, and $\Delta \log (\text{O}/\text{H})$ for each baxel in the following way. Taking stellar age, for example, $\Delta \log \text{age}$ is the difference in age of a baxel from the median age of all baxels (controls) within a window of the same total stellar mass (M_*), local mass density (Σ_*) and position (R) within their galaxies. The windows are 0.05, 0.05 and 0.2 for $\log M_*/M_\odot$, $\log \Sigma_*/(M_\odot \text{kpc}^{-2})$ and R/kpc respectively. (These windows are iteratively grown by 0.05, 0.05 and 0.1 if the number of control baxels is less than 10, but in practice, this happens for a few % of the baxels.) A typical galaxy of any mass will have $\Delta \log \text{age} = 0$ at all R by definition. $\Delta \log \text{sSFR}$ and $\Delta \log (\text{O}/\text{H})$ are computed in the same way. ($\Delta \log \text{SFR}$ will be the same as $\Delta \log \text{sSFR}$ due to our controlling for Σ_* .) Note that in the computation of $\Delta \log \text{age}$, the sample of “good” age baxels are used for the pool of controls as defined in §2.3, while for $\Delta \log \text{sSFR}$ and $\Delta \log (\text{O}/\text{H})$, the pool of controls are the “good” gas baxels defined in §2.4.

Thus “gradients” and “profiles” provide complementary information regarding the structure of galaxies. Gradients are a single number per galaxy in each of age, sSFR and O/H, and are the measurements presented in the left panels of Figs. 3-8 (discussed below). The profiles of our “ Δ ” quantities are computed as an average for a population of galaxies, and captures more radial information. Profiles are the measurements presented in the right panels of Figs. 3-8 (discussed below).

3 THE GROWTH OF GALAXIES ON $\Sigma_{*,1\text{kpc}}-M_*$ RELATION

3.1 The $\Sigma_{*,1\text{kpc}}-M_*$ as a Map for Galaxy Growth

Our goal as stated in the introduction was to determine the stellar age gradients of galaxies as a function of position on the $\Sigma_{*,1\text{kpc}}-M_*$ relation. The distribution of galaxies in the $\Sigma_{*,1\text{kpc}}-M_*$ plane was first studied by Fang et al. (2013) who noted that quiescent galaxies lie on a tight ridge-line in this parameter space. We reproduce this relation for reference in Fig. 2 (red contours) for the quiescent (Q) galaxies in the DR7 SDSS (defined as having global sSFR $< 10^{-11} \text{yr}^{-1}$, where the global sSFR is from the Brinchmann et al. 2004 DR7 catalogue, about 15000 galaxies). Star-forming (SF) galaxies (blue contours, defined as having global sSFR $> 10^{-11} \text{yr}^{-1}$, about 39000 galaxies) at the same mass have a wider range of $\Sigma_{*,1\text{kpc}}$ than quiescent galaxies, but their $\Sigma_{*,1\text{kpc}}-M_*$ sequence is still relatively tight (scatter ~ 0.3 dex in M_*). Fang et al. (2013) noted that the quiescent relation is offset to higher $\Sigma_{*,1\text{kpc}}$ (at the same M_*) compared to the star-forming relation and interpreted this as a mass-dependent density threshold for quenching. This offset is one manifestation of the morphology-quiescence relation. Barro et al. (2017) showed that both the star-forming and quiescent sequences evolve modestly with redshift, their zero-points decreasing by $\lesssim 0.3$ since $z \sim 3$.

Star forming galaxies are expected to increase their

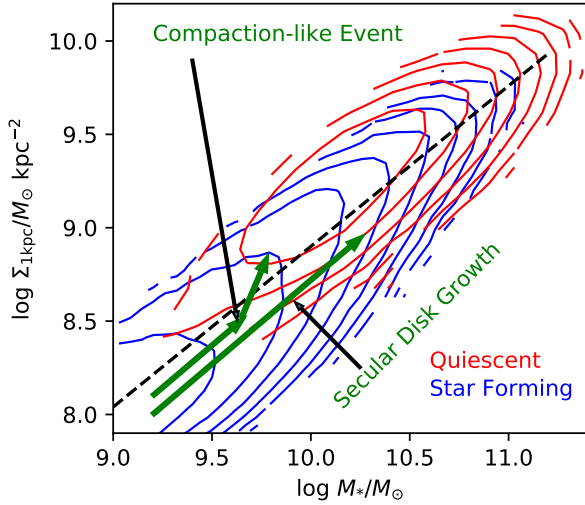


Figure 2. The surface density within 1 kpc as a function of total stellar mass for isolated quiescent galaxies (red) and star forming galaxies (blue) in the SDSS DR7 within $0.01 < z < 0.07$. The contours are weighted by the $1/V_{\text{max}}$ multiplied by the inverse of the spectroscopic completeness. The dashed black line divides the galaxies into “compact” and “diffuse” cores to be used in later analyses. The green arrows qualitatively indicate the expected evolutionary paths of galaxies growing in the two modes indicated. The secular disk growth track increases in M_* faster than in $\Sigma_{*,1\text{kpc}}$, so the slope of this growth should be $\lesssim 1$ (the slope of the arrow is about 0.9). The compaction track may start off on the secular track, but when a galaxy experiences a compaction event this leads to an increase in $\Sigma_{*,1\text{kpc}}$ that is faster than in M_* , and brings a galaxy to the upper part of the diagram.

mass by a factor of ~ 20 since $z \sim 3$ (van Dokkum et al. 2010; Behroozi et al. 2013; Moster et al. 2013; Papovich et al. 2015) which is much larger than the scatter of the $\Sigma_{*,1\text{kpc}}-M_*$ scaling relation and the evolution of the zero-point. Thus Barro et al. (2017) argued that galaxies likely evolve along the SF relation which has a slope of ~ 0.9 at all z (our best fit for the SDSS DR7 has a slope of 0.86). Chen et al. (in preparation) demonstrate from the growth of halos that the slope of the evolutionary track of a single galaxy is expected to be closer to 0.7, i.e., shallower than the $\Sigma_{*,1\text{kpc}}-M_*$ relation for the population as a whole. Either way, the slope of the secular evolutionary track is predicted to be $\lesssim 1$, meaning that the inner kpc grows more slowly than the galaxy as a whole, which is consistent with inside-out disk growth through galaxy-wide star formation (e.g., Fall & Efstathiou 1980; van den Bosch 1998; Kepner 1999; Lilly & Carollo 2016). We might therefore expect these SF galaxies to have negative age gradients (older centres), since they have built their centres in the distant past, but have continued to grow a disk.

However, SF galaxies could deviate from this secular disk growing mode if they experience a compaction-like event that triggers gas inflow and the growth of the bulge/core. A compaction event would lead to the galaxy being offset above the SF sequence of the $\Sigma_{*,1\text{kpc}}-M_*$ relation, such that its central density is high for its M_* . Indeed, such evolution is observed in hydrodynamical simulations,

where galaxies evolve along the SF sequence in $\Sigma_{*,1\text{kpc}}-M_*$ until a major dissipative event pushes their evolution upwards along pathways that are steeper than the SF sequence (see Fig. 19 of Zolotov et al. 2015 and Fig. 5 of Barro et al. 2017). Such compaction events are triggered by major mergers, disk instabilities or any other mechanism that brings significant amounts of gas to the centre of the galaxy resulting in enhanced star-formation in the centre (Dekel et al. 2009; Zolotov et al. 2015). Although the most violent and gas rich compaction events are prevalent at high z , at later times gas-rich processes may also include longer-lived bar instabilities (see Lin et al. 2017) and minor mergers. Since these lower- z events are still gas-rich and dissipative, we consider them “compaction-like” (see §5 for a discussion of the nature of low- z “compaction”). Galaxies experiencing these compaction-like events have added new stars to their centres (e.g., Ellison et al. 2018). Thus at the end of their steeper trajectories in the $\Sigma_{*,1\text{kpc}}-M_*$ plane, their age gradients should be more positive than expected given secular inside-out growth.

In light of the expected evolution of SF galaxies in the $\Sigma_{*,1\text{kpc}}-M_*$ diagram for these two growing modes, we divided the galaxies into those with “compact” and “diffuse” cores using the dashed black line Fig. 2. The equation of the line is $\log \Sigma_{*,1\text{kpc}} = 0.86(\log M_* - 10) + 8.9$ which is the best-fit line to the SF galaxies, offset upward by 0.1 dex so that the Q population also has sufficient numbers of “diffuse” cores. Our results are not qualitatively sensitive to reasonable variations in the placement of this line.

3.2 Age Gradients and Profiles

In order to test whether galaxies on/above the SF sequence of the $\Sigma_{*,1\text{kpc}}-M_*$ relation show different age gradients, we show the age gradients (§2.5) of MaNGA galaxies as a function of the $\Sigma_{*,1\text{kpc}}-M_*$ relation in Fig. 3. Fig. 3 shows only SF galaxies from MaNGA, with the SF and Q contours for the general SDSS DR7 population (reproduced from Fig. 2) in the background for reference. The points in Fig. 3a show the individual MaNGA galaxies colour-coded by their age gradient. Though there is some scatter, Fig. 3a shows that at fixed stellar mass, star-forming galaxies with denser cores (higher $\Sigma_{*,1\text{kpc}}$) tend to have positive age gradients (younger centres) while negative age gradients (older centres) are characteristic of galaxies lying lower on the $\Sigma_{*,1\text{kpc}}-M_*$ relation. The red points, for example, (those with gradients of $\log \text{age} \lesssim -0.1$) are almost all below the black line. This is consistent with an evolutionary picture that includes both inside-out disk growth characterized by negative gradients, and compaction-like processes characterized by more positive age gradients. The latter brings galaxies to the upper part of the $\Sigma_{*,1\text{kpc}}-M_*$ relation via an evolutionary trajectory that is steeper than the slope of the population’s $\Sigma_{*,1\text{kpc}}-M_*$ relation. The difference between age gradients is strongest at the lowest masses, but even for the most massive SF galaxies, those with denser cores (higher $\Sigma_{*,1\text{kpc}}$ at fixed M_*) tend to have more positive age gradients than those with lower $\Sigma_{*,1\text{kpc}}$.

We caution here that the numerical scale on the colour bars in Fig. 3a is somewhat sensitive to the stellar population models used. We show here the result of using the E-MILES templates. Using the Maraston & Strömbäck (2011) models,

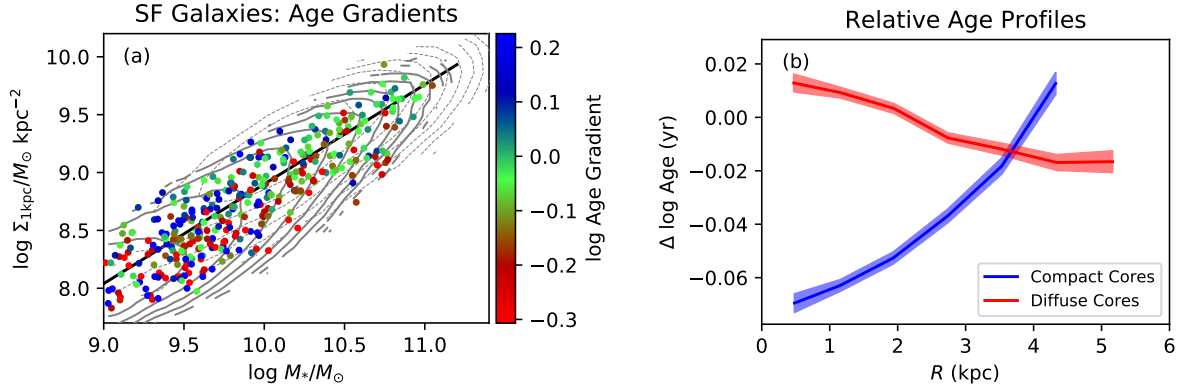


Figure 3. (a) The age gradient as a function of the $\Sigma_{*,1\text{kpc}}-M_*$ relation for the star forming population. The grey contours represent the SF and Q populations in the SDSS DR7 sample, and the points are the MaNGA galaxies. (b) The mean relative age profiles (smoothed over adjacent bins) for galaxies above (blue) and below (red) the black line shown in panel (a). Galaxies with compact cores (relative to their M_*) have relatively younger centres compared to their outskirts while galaxies with lower $\Sigma_{*,1\text{kpc}}$ have older centres.

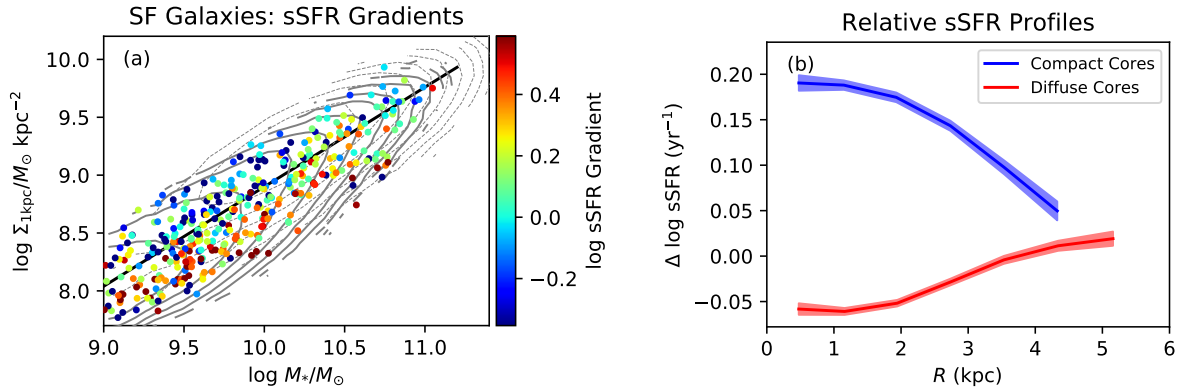


Figure 4. (a) The sSFR gradient as a function of the $\Sigma_{*,1\text{kpc}}-M_*$ relation for the star forming population. The grey contours represent the SF and Q populations in the SDSS DR7 sample, and the points are the MaNGA galaxies. (b) The mean relative sSFR profiles (smoothed over adjacent bins) for galaxies above (blue) and below (red) the black line shown in panel (a). Galaxies with compact cores (relative to their M_*) have centrally peaked sSFR while galaxies with lower $\Sigma_{*,1\text{kpc}}$ form stars in their outskirts.

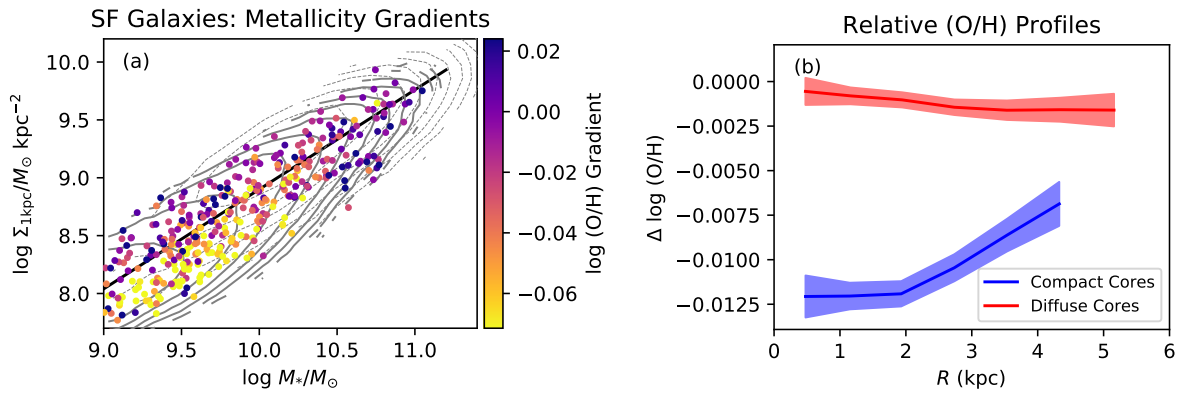


Figure 5. (a) The gradient of $12 + \log(\text{O}/\text{H})$ as a function of the $\Sigma_{*,1\text{kpc}}-M_*$ relation for the star forming population. The grey contours represent the SF and Q populations in the SDSS DR7 sample, and the points are the MaNGA galaxies. (b) The mean relative $\log(\text{O}/\text{H})$ profiles (smoothed over adjacent bins) for galaxies above (blue) and below (red) the black line shown in panel (a). Galaxies with compact cores (relative to their M_*) have relatively metal-poor gas in their centres while galaxies with lower $\Sigma_{*,1\text{kpc}}$ have O/H profiles that mildly decrease with radius.

for example, produces qualitatively similar trends, but the age gradients are always negative. What is consistent between the models is that SF galaxies with denser cores have *more positive* age gradients than those with lower $\Sigma_{*,1\text{kpc}}$ at the same mass.

A complementary demonstration of the different age gradients of galaxies with different mass profiles is shown in Fig. 3b. Here, we define galaxies with “compact” or “diffuse” cores as those that lie above (high $\Sigma_{*,1\text{kpc}}$ at a given M_*) or below (low $\Sigma_{*,1\text{kpc}}$ for a given M_*) the line through the SF sequence shown in Fig. 2 (and re-drawn in Fig. 3a). Fig. 3b shows the (smoothed) profiles of $\Delta \log \text{age}$ (§2.5), which quantify whether a given baxel has a larger or smaller age than expected given its stellar mass density and radial position, as well as the M_* of its host galaxy. Note that although only galaxies with at least 10 good baxels (required to define a gradient) are shown on panel (a), all good baxels (criteria in §2.3) from all star-forming galaxies are represented in panel (b) in order to compute the mean profiles of $\Delta \log \text{age}$. The error on the mean $\Delta \log \text{age}$ is represented by the width of the shaded region. We visually checked the profiles of individual galaxies and confirm that these average profiles (and all the following profiles) accurately represent the overall radial trends of most individual galaxies in these subsamples.

Fig. 3b shows that baxels in the centres of galaxies with dense cores are young (have negative $\Delta \log \text{age}$) relative to the typical baxel of the same mass density, position and host galaxy mass. Conversely, galaxies with diffuse cores are relatively older in their centres. The trends exhibited by the age profiles are therefore consistent with the trends captured by the age gradients, and with the evolutionary picture discussed above. In other words, some galaxies grow their disks inside-out and have older centres, while others experience a compaction-like event that adds new stars to their centres, increases their core density and places them on the upper part of the $\Sigma_{*,1\text{kpc}}-M_*$ diagram.

3.3 sSFR Gradients and Profiles

In the previous sub-section (Fig. 3), we demonstrated that SF galaxies with compact cores (at fixed M_*) have relatively young central ages compared to their outskirts, while SF galaxies with diffuse cores have older central ages. In this sub-section we test whether these differences in age gradients and $\Delta \log \text{age}$ profiles are also seen in the current star formation rates. In Fig. 4a, we once again show the distribution of our MaNGA sample on the $\Sigma_{*,1\text{kpc}}-M_*$ plane, but now colour coded by their sSFR gradients. The corresponding profiles of relative sSFR are shown in Fig. 4b, comparing galaxies with compact vs diffuse cores. Fig. 4 is therefore analogous to Fig. 3 except that the sSFR gradients and the profiles of $\Delta \log \text{sSFR}$ are computed only from baxels that meet our star-forming criteria (§2.4 and 2.5).

Panel (a) of Fig. 4 shows that the sSFR gradients tend to be negative (high sSFR in the centres) for galaxies with compact cores. These galaxies lie in the region of the $\Sigma_{*,1\text{kpc}}-M_*$ diagram where the age gradients (Fig. 3a) tend to be positive, and where galaxies are expected to evolve to after compaction-like events. Panel (b) confirms that the sSFR is enhanced in the centres of galaxies with dense cores. Thus the relatively younger centres of galaxies with dense

cores are experiencing centrally-concentrated star formation consistent with these galaxies undergoing a compaction-like event. Galaxies with diffuse cores have very different star formation profiles; sSFR gradients tend to be positive (higher sSFR in the outskirts - panel a), and their sSFR profiles are suppressed in their centres.

3.4 O/H Gradients and Profiles

Lastly, we show the gradients of gas phase metallicity and the corresponding profiles of relative metallicity in Fig. 5a and b using only star-forming baxels (§2.4 and 2.5) to ascertain the nature of the gas feeding the star formation. Fig. 5a shows that the upper part of the $\Sigma_{*,1\text{kpc}}-M_*$ SF sequence (galaxies with compact cores) is dominated by more positive gas metallicity gradients (lower metallicities in their centres). Panel b confirms that the centres of star-forming galaxies with compact cores, where the stars are relatively young and the sSFR is enhanced, the gas fueling the star formation is deficient in metals. In contrast, star forming baxels in galaxies with diffuse cores have higher relative gas metallicities compared to galaxies with compact cores, and weakly declines with radius.

Taken together, the variation in galaxies’ central mass density at a fixed M_* (Fig. 2), and their contrasting profiles of age, sSFR and O/H (Figs. 3-5), indicate that galaxies do not follow a single growth pathway. At the very least, the data are consistent with two complementary routes. On one path galaxies grow inside-out by adding stars preferentially to the outskirts. Their total mass increases faster than the mass in their cores and they evolve along the lower part of the star-forming sequence in the $\Sigma_{*,1\text{kpc}}-M_*$ diagram. In addition, some galaxies experience a compaction-like event that grows the core through centrally concentrated star formation fed by gas that is relatively low in metallicity. These galaxies lie in the upper part of the star-forming sequence in the $\Sigma_{*,1\text{kpc}}-M_*$ diagram since their core mass has increased.

4 THE $\Sigma_{*,1\text{kpc}}-M_*$ RELATION OF THE QUIESCENT POPULATION

As noted in §3 and shown in Fig. 2, the $\Sigma_{*,1\text{kpc}}-M_*$ relation for quiescent galaxies lies above the relation for the star-forming galaxies and has a shallower slope (~ 0.7). However there is substantial overlap between the star-forming and quiescent relations. For a galaxy to become quenched, it must evolve along the star-forming relation until it reaches the region of $\Sigma_{*,1\text{kpc}}-M_*$ space that is covered by the quiescent relation, which includes a large portion of the upper part (high M_* as well as $\Sigma_{*,1\text{kpc}}$) of the star-forming relation. Thus galaxies can potentially reach the quiescent relation via either of the growth routes discussed in §3: the lower “inside-out” growth route, or the upper “compaction” route. In this section, we investigate the presence of signatures of either route in the stellar ages, star formation rates and gas metallicities of the quiescent population. Figs. 6, 7 and 8 are analogous to Figs. 3, 4 and 5, except for quiescent, rather than star forming galaxies. We discuss each of these figures in turn.

Fig. 6 shows the gradients of stellar age for quiescent

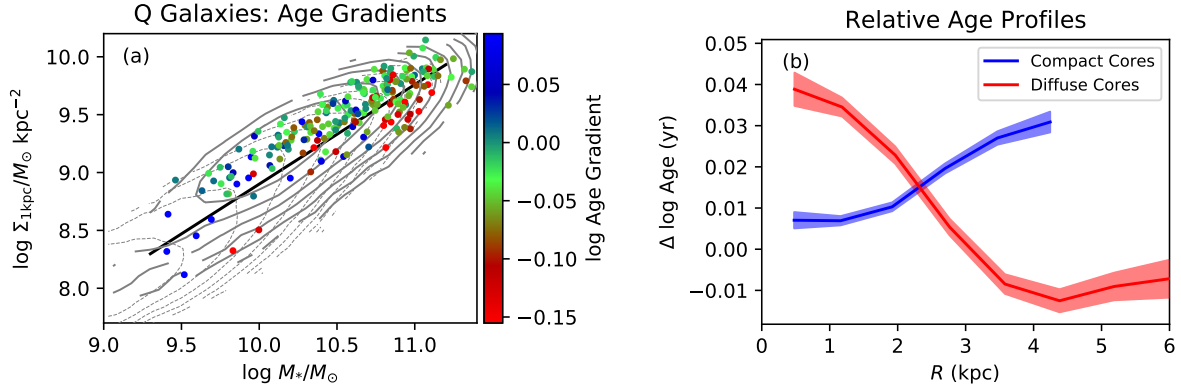


Figure 6. (a) The age gradient as a function of the $\Sigma_{*,1\text{kpc}}-M_*$ relation for the quiescent population in MaNGA (points). The grey contours represent the SF and Q populations in the SDSS DR7. (b) The mean relative age profiles (smoothed over adjacent bins) for galaxies above (blue) and below (red) the black line shown in panel (a). Quiescent galaxies with more compact cores (relative to their M_*) are relatively younger in their centres than galaxies with lower $\Sigma_{*,1\text{kpc}}$.

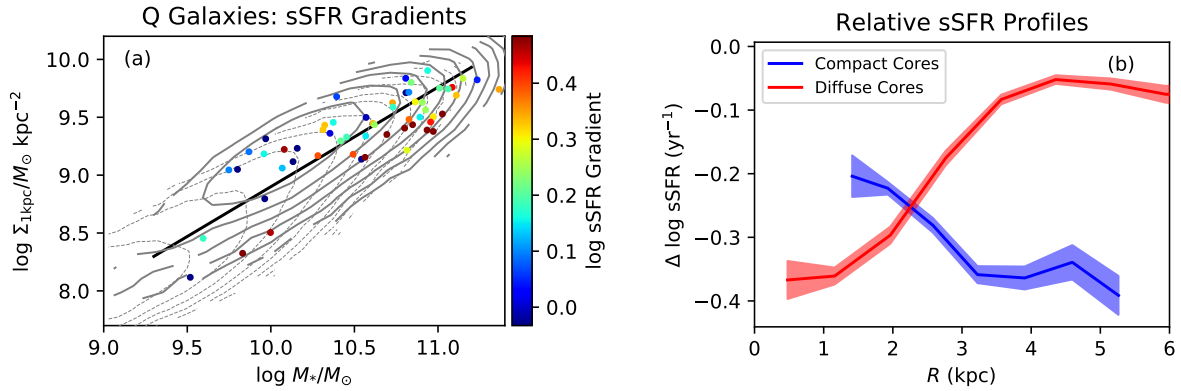


Figure 7. (a) The sSFR gradient as a function of the $\Sigma_{*,1\text{kpc}}-M_*$ relation for the quiescent population in MaNGA (points). The grey contours represent the SF and Q populations in the SDSS DR7. (b) The mean relative sSFR profiles (smoothed over adjacent bins) using only star-forming baxels in galaxies above (blue) and below (red) the black line shown in panel (a). Residual star formation in quiescent galaxies with compact cores is centrally peaked, suggesting uniform quenching. Residual star formation in galaxies with diffuse cores are more suppressed in their centres, suggesting inside-out quenching.

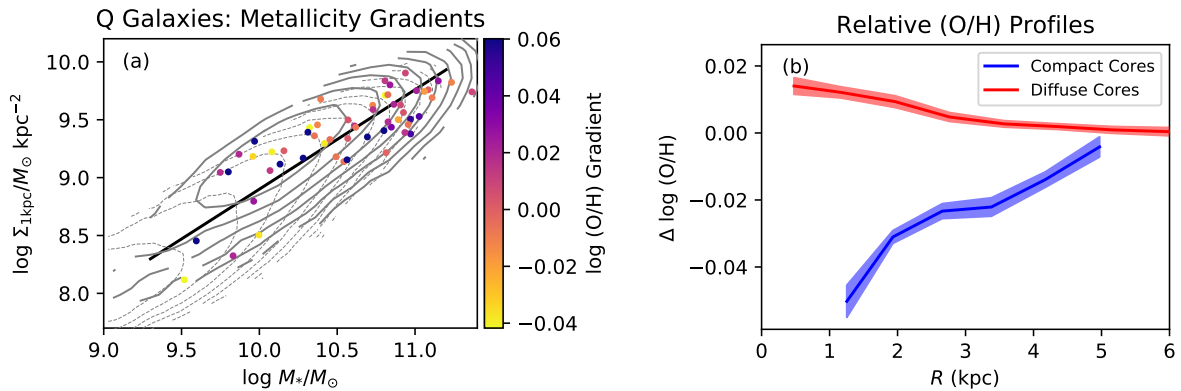


Figure 8. (a) The gradient of $12 + \log(\text{O}/\text{H})$ as a function of the $\Sigma_{*,1\text{kpc}}-M_*$ relation for the quiescent population in MaNGA (points). The grey contours represent the SF and Q populations in the SDSS DR7. (b) The mean relative $\log(\text{O}/\text{H})$ profiles (smoothed over adjacent bins) using star-forming baxels in galaxies above (blue) and below (red) the black line shown in panel (a). Galaxies with compact cores have relatively metal-poor gas in their centres while galaxies with lower $\Sigma_{*,1\text{kpc}}$ are more metal-poor in their outskirts.

galaxies in the $\Sigma_{*,1\text{kpc}}-M_*$ plane. Panel (a) of this figure shows that quiescent galaxies have mostly negative age gradients (older centres). However, we note again that numerical scale on the colour bars is somewhat sensitive to the input stellar population models. For example, the age gradients determined from the Firefly fitting software (using the Maraston & Strömbäck 2011 models - see Goddard et al. 2017) produce strongly positive age gradients for most quiescent galaxies. However, the *relative* gradients are consistent among all models: galaxies with higher $\Sigma_{*,1\text{kpc}}$ have *more positive* age gradients than those with lower $\Sigma_{*,1\text{kpc}}$ (at fixed M_*). This is seen as a gradient in the colours of the points in Fig. 6a.

To demonstrate the difference in relative gradients between galaxies with different core densities, we show the mean relative age profiles in Fig. 6b comparing galaxies above (“compact”) and below (“diffuse”) the black line in panel (a), which is the same line used to divide compact and diffuse cores for the SF galaxies. Although the line lies below the main bulk of Q galaxies, it happens to roughly divide the red points (log age gradient $\lesssim -0.05$) from the green and blue points (log age gradient $\gtrsim -0.05$) in panel (a), suggesting a relation with the SF evolutionary paths discussed in §3 (this relation will be discussed in §5). The quantity on the y -axis of panel (b) is again a measurement of the offset in age of a baxel compared to the expected age of similar baxels. Fig. 6a confirms that quiescent galaxies with dense cores (high $\Sigma_{*,1\text{kpc}}$ relative to their M_*) have positive relative age gradients while those with more diffuse cores have negative gradients.

We remind the reader that, in order to facilitate comparison with other studies, quiescent galaxies were defined using the commonly used criterion $\log \text{sSFR}/\text{yr}^{-1} < -11$, where the sSFR is the global value (not the baxel value) from the widely used MPA-JHU DR7 catalogue (Brinchmann et al. 2004). Despite their overall “quiescent” nature, over half of these galaxies have residual emission lines from individual star-forming regions when observed with the MaNGA IFU, although their total sSFR inferred from these lines is consistently low. There are enough of these star-forming baxels to compute gradients in sSFR and O/H, but the number that fulfill our 10-baxel requirement for a gradient (§2.5) is only about $\sim 27\%$ of quiescent galaxies. However, mean profiles of $\Delta \log \text{sSFR}$ and $\Delta \log (\text{O}/\text{H})$ are computed from all star-forming baxels in all quiescent galaxies. The gradients and profiles of sSFR and gas metallicity are shown in Figs. 7 and 8.⁶

Figs. 7 and 8 show that for those quiescent galaxies with residual star formation, galaxies with compact cores have suppressed sSFR everywhere, but preferentially in the outskirts. The gas metallicities of the same compact quiescent galaxies are low in the centres. In contrast, quiescent galax-

ies with diffuse cores have suppressed sSFR and enhanced gas metallicity in their centres compared to their outskirts.

Our findings indicate that quiescent galaxies with different core densities have different gradients and profiles of stellar age, sSFR and gas metallicity. Aside from the vertical scales, the qualitative differences between galaxies with compact vs. diffuse cores roughly mirror the differences seen in the star-forming galaxies we presented in the previous section. The presence of both positive and negative profiles in age, sSFR and O/H amongst the quiescent population indicate that different evolutionary pathways have led them into quiescence.

5 DISCUSSION: THE GROWTH AND QUENCHING OF GALAXIES

Our study was motivated by the question of distinguishing between core-building “compaction”-like events (Zolotov et al. 2015) and progenitor effects of secular inside-out growth (Lilly & Carollo 2016) as the reason for the morphology-quiescence relation. Through our study of the age, sSFR and gas phase metallicity gradients and radial profiles as a function of position on the $\Sigma_{*,1\text{kpc}}-M_*$ diagram, we have uncovered evidence pointing to at least two pathways of growth consistent with 1) compaction-like core-building events and 2) secular inside-out growth by global star formation. The cores of compact (high $\Sigma_{*,1\text{kpc}}$ at given M_*) star-forming galaxies are relatively young, enhanced in sSFR, and deficient in metals compared to their outskirts. In contrast, the centres of galaxies with diffuse cores (low $\Sigma_{*,1\text{kpc}}$ for their M_*) are characterized by relatively older stellar ages, lower sSFR and higher O/H. We showed that the quiescent galaxies also have age, sSFR and gas metallicity profiles that depend on their central stellar mass densities. Like the SF population, quiescent galaxies with compact cores differ from those with diffuse cores in their stellar ages, sSFR and gas metallicities (when gas is present). Our results suggest that both modes of growth (secular and compaction) contribute to the quiescent population and that the morphology-quiescence relation results from both modes.

Multiple modes of quenching isolated or central galaxies (usually a fast and slow mode) have been suggested in the literature before (Barro et al. 2013; Schawinski et al. 2014; Woo et al. 2015), and may correspond to the quenching after the compaction-like and secular growth modes argued for here. Evidence for multiple *growing* modes are only now emerging in recent research. Liu et al. (2018) divided the galaxies in MaNGA essentially by age gradient (more precisely, D4000 gradient) and find that the galaxies populate different spatially resolved SFR- M_* relations. Those with older centres have shallower SFR- M_* relations than those with younger centres (see also the recent study by Hall et al. 2018). In other words, galaxies with older centres have suppressed SFR in spaxels of the highest Σ_* (i.e., in their centres) compared with galaxies with younger centres. Our study has explicitly linked these trends of age and SFR gradients with the compactness of the cores on these two growing modes.

If our interpretation of two growing modes is correct, then we can make a few inferences about quenching which we unpack below. Since our division between galaxies with

⁶ To compute the average profiles in these plots, we included only those galaxies with median $\Delta \log \text{sSFR} > -0.8$ for Fig. 7b and median $\Delta \log (\text{O}/\text{H}) > -0.1$ for Fig. 8b. This is because there were a few galaxies far below these plots that were artificially skewing the average (and median) profiles. We checked that the profiles of the majority of individual galaxies in these subsamples follow the same trends (increasing or decreasing with radius) as indicated by the mean profiles shown in these plots.

compact and diffuse cores was the same in our analyses of both SF and Q galaxies, for the purposes of the ensuing discussion, we will assume that the position on the $\Sigma_{*,1\text{kpc}}-M_*$ diagram for the Q galaxies (i.e., having compact vs diffuse cores) is the end point of the two growing pathways. In essence, this means that neither $\Sigma_{*,1\text{kpc}}$ nor M_* evolves much after quenching. This is not an unreasonable assumption given that the quiescent sequence significantly overlaps the SF sequence in this diagram. Furthermore, since it is difficult to decrease $\Sigma_{*,1\text{kpc}}$, any movement towards the “diffuse core” part of the diagram after compaction would likely require an increase in M_* by at least a factor of two (a horizontal movement), which may be difficult to achieve through merging without increasing $\Sigma_{*,1\text{kpc}}$.

5.1 The Compaction-like Evolutionary Track

In the growing mode that involves a compaction-like event, low-metallicity gas is funnelled to the central regions of a galaxy. This gas fuels a centrally concentrated burst of star formation (Fig. 4b) that increases their $\Sigma_{*,1\text{kpc}}$ faster than their M_* , bringing them to the upper part of the $\Sigma_{*,1\text{kpc}}-M_*$ sequence (Fig. 2). Classical compaction events resulting from violent disk instabilities are a high- z phenomenon (Zolotov et al. 2015), triggered by low-metallicity cosmic streams (Dekel et al. 2009; Cresci et al. 2010). However, our study is limited to $z \sim 0$ galaxies (and thus we have been calling this track “compaction-like”). Furthermore, we have observed centrally concentrated star formation in the upper $\Sigma_{*,1\text{kpc}}$ track occurring in the last few Myr (through H α emission). What is the nature of this low- z phenomenon characterized by the gradients and profiles of stellar age, sSFR and gas metallicity?

One possibility is major mergers. The metal-deficient gas in the centres of these galaxies (Fig. 5b) is reminiscent of what has been seen in galaxies expected to be currently under-going a merging event (low central O/H, and/or flatter gradients: Kewley et al. 2010; Scudder et al. 2012; Ellison et al. 2013; Thorp et al. 2018), as well as galaxies with enhanced central star formation rate (Ellison et al. 2018). Furthermore, $\Sigma_{*,1\text{kpc}}$ correlates tightly with the central velocity dispersion at fixed M_* (Fang et al. 2013) which may suggest a more active merger history in the upper part of the $\Sigma_{*,1\text{kpc}}-M_*$ sequence compared to the lower part.

The recent study of Lin et al. (2017) hints at another possible low- z “compaction” mechanism. These authors study the inner regions of 57 star-forming disk galaxies in CALIFA and find that the centres of 17 have a drop in D4000 (younger ages) and an enhancement of EW(H α) (sSFR), similar to our findings for galaxies on the upper part of the $\Sigma_{*,1\text{kpc}}-M_*$ diagram. They found that most of these are barred galaxies, suggesting that low- z “compaction” may involve bar instabilities. However, simulations predict *higher* gas phase metallicities in barred galaxies (Martel et al. 2018). Indeed Ellison et al. (2011) found that although barred galaxies in the SDSS have elevated SFR in their centres, their gas metallicities are higher than unbarred galaxies in contrast to our findings of lower metallicities in the centres of galaxies on the compaction track. Ellison et al. (2011) speculated that their findings implied that bars are long-lived phenomenon. Therefore they may be a completely different population from our MaNGA galaxies with high

$\Sigma_{*,1\text{kpc}}$ (for their M_*). Clearly, further study is required to ascertain the nature of low- z compaction.

As to the manner of the quenching after the compaction-like track, we have observed that the sSFR profiles on the compaction-like track are overall suppressed after quenching, but retain more or less the same decreasing slope (compare the blue curves of Figs 4b and 7b). In other words, under the assumption that the blue profiles in Figs 4b and 7b can be connected as an evolutionary sequence, the suppression of star formation after the compaction-like track happens roughly uniformly across the whole galaxy. This may be an indication of the timescale of the quenching, which occurs too quickly to be registered as a change in the sSFR profile. Indeed, Wang et al. (2018) recently found that the HI content and gas depletion time for SF galaxies with compact cores are reduced by a factor of two compared to those with diffuse cores.

One popular possibility for quenching galaxies on the compaction track is AGN feedback (Bell 2008; Bluck et al. 2014; Terrazas et al. 2016, 2017; Kocevski et al. 2017). AGN require a fuel source, and this is naturally provided by the same dissipative compaction-like processes which funnel gas toward the centres of galaxies (gas-rich mergers and gravitational disc instabilities). The higher velocity dispersions in galaxies with higher $\Sigma_{*,1\text{kpc}}$ (Fang et al. 2013) may point to the importance of black hole growth (via the $M_{\text{BH}} - \sigma$ relation - Kormendy & Ho 2013) during the compaction event, and then later for quenching (as argued for example by Bluck et al. 2016). In fact, Kocevski et al. (2017) showed that for galaxies at $z \sim 2$, the X-ray detected AGN fraction peaks for galaxies of high sSFR and high $\Sigma_{*,1\text{kpc}}$, exactly in the region of the sSFR- $\Sigma_{*,1\text{kpc}}$ diagram where energy injection is needed to quench galaxies (their Fig. 8 uses U-V colour instead of sSFR). This motivated the question of whether the AGN fraction peaks in the ($z \sim 0$) $\Sigma_{*,1\text{kpc}}-M_*$ diagram where we propose galaxies evolve due to compaction-like events. We show this fraction as a function of $\Sigma_{*,1\text{kpc}}-M_*$ plane in Fig. 9 using WISE-detected AGN for SF galaxies. WISE detections are matched to SDSS DR7 objects if the angular separation is less than 6". The AGN fraction is then computed from the fraction of WISE detections with $W1-W2$ colour greater than 0.77, which is the 75% completeness criterion of Assef et al. (2018). We show WISE-selected AGN rather than emission-line AGN because the former method detects AGN obscured by dust, which is more prevalent in processes such as mergers that funnel gas to the centre and can hide emission-line signatures of AGN (Mateos et al. 2013; Blecha et al. 2018).

Fig. 9 shows that the WISE selected AGN fraction for SF galaxies peaks in the upper regions of the $\Sigma_{*,1\text{kpc}}-M_*$ plot, i.e., with high $\Sigma_{*,1\text{kpc}}$. This is also where the centres of galaxies are relatively young, sSFR is enhanced, and the gas metallicity is low, pointing to a possible connection between AGN and the compaction-like evolutionary path. WISE AGN tend to correspond to galaxies with high SFR (Ellison et al. 2016; Cowley et al. 2016; Azadi et al. 2017), indicating that AGN and high SFR might be tracing the same process. In particular, a centrally concentrated boost of SFR tracing elevated nuclear accretion as may happen in mergers would be exemplary of compaction-like core-building. Thus AGN are a natural candidate for the quenching mechanism that suppresses sSFR quickly everywhere.

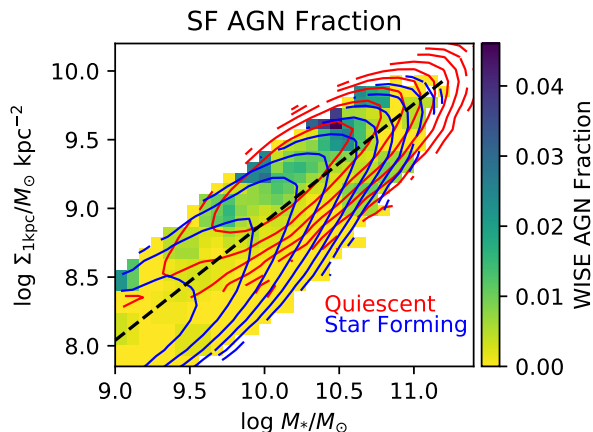


Figure 9. The $\Sigma_{*,1\text{kpc}}-M_*$ diagram colour-coded with the WISE-detected AGN fraction for SF galaxies. WISE detections are matched to SDSS DR7 objects if the angular separation is less than $6''$. The AGN fraction is then computed from the fraction of WISE detections with $W1-W2$ colour greater than 0.77, which is the 75% completeness criterion of Assef et al. (2018). The black dashed line indicates our division between “compact” and “diffuse” cores. The WISE-detected AGN fraction peaks in the upper region of the $\Sigma_{*,1\text{kpc}}-M_*$ diagram (galaxies with compact cores), where the profiles of stellar age, sSFR and gas metallicity are characteristic of compaction-like events.

5.2 The Secular Disk-Growing Mode

When disks are growing inside-out through the successive addition of gas in ever-growing exponential disks (or growing angular momentum), sSFR is highest in the outskirts (Fig. 4). M_* grows faster than $\Sigma_{*,1\text{kpc}}$ and galaxies evolve along the lower part of the $\Sigma_{*,1\text{kpc}}-M_*$ relation (Fig. 2). Gas-phase metallicity is higher in the centres than in the outskirts (Fig. 5a) indicating that mixing is relatively unimportant. When these galaxies reach the quenched region of the $\Sigma_{*,1\text{kpc}}-M_*$ diagram, sSFR is suppressed most dramatically in the centres, as indicated by the steeper sSFR profiles after quenching (compare the red curves in Figs 4b and 7b). In other words, the quenching process after secular disk growth occurs “inside-out”. This is consistent with several other observations of inside-out quenching (Tacchella et al. 2016; González Delgado et al. 2016; Ellison et al. 2018; Belfiore et al. 2018; Liu et al. 2018). Though we have not explicitly studied timescales here, the secular disk growing mode is expected to be a quieter and longer-lived mode than the compaction-like track. Wang et al. (2018) find that the depletion time is twice as long for galaxies with low $\Sigma_{*,1\text{kpc}}$ than galaxies with higher $\Sigma_{*,1\text{kpc}}$ (at fixed M_*) supporting the slower evolution of the inside-out mode.

Just as in the compaction case, the quenching mechanism after the inside-out growing mode could very well be AGN. The central black hole can still accrete (slowly) as the disk grows, until a critical mass is reached (e.g., Terrazas et al. 2016, Chen et al., in prep.) triggering perhaps the “radio/maintenance mode” (Croton et al. 2006) of AGN in a hot halo. Regardless of the mechanism, the gas in the centres is likely depleted/removed first. In order to constrain scenarios further, measurements are needed of radial profiles

of the depletion time, and/or the fraction of low-luminosity AGN, as a function of position on the $\Sigma_{*,1\text{kpc}}-M_*$ diagram.

If the quiescent galaxies with lower $\Sigma_{*,1\text{kpc}}$ are indeed the end point of the evolution of the inside-out disk growth track, the fact that these quiescent galaxies are younger than those with higher $\Sigma_{*,1\text{kpc}}$ indicates that this quenching track may be more dominant today than the compaction track. Yet, the number of quiescent galaxies with at least 10 star-forming baxels is roughly the same in the low- and high- $\Sigma_{*,1\text{kpc}}$ regions of the quiescent $\Sigma_{*,1\text{kpc}}-M_*$ diagram (Fig. 7a). These findings imply that though the compaction track and the secular track may have respectively decreased and increased in importance over time, the quenching that occurs after the compaction track still continues to quench about half of galaxies today.

5.3 Caveats

We have interpreted our results as indicating (at least) two galaxy growing modes, both of which contribute to the morphology-quiescence relation. However, one of the difficulties in inferring evolution from today’s populations is that we observe a snapshot that includes the end result of recent evolution as well as quenching that occurred long ago. The quiescent population today is mostly very old ($\gtrsim 10$ Gyr) and their evolutionary pathways will not in general be the same as those by which galaxies evolve today.

For example, consider the following argument for an alternate interpretation of the age gradients in quiescent galaxies. Tacchella et al. (2017) showed (through photometric SED fitting) that quiescent galaxies with compact cores are *older* than those with lower $\Sigma_{*,1\text{kpc}}$ at the same mass, which is expected if compactness is an indication of the time of quenching (van Dokkum & Franx 2001; Carollo et al. 2013; Lilly & Carollo 2016) rather than compaction. We have confirmed spectroscopically that galaxies with high $\Sigma_{*,1\text{kpc}}$ for their M_* are indeed older overall.⁷ Furthermore, we have found that the age gradients for quiescent galaxies are negative (which is disputed by Goddard et al. 2017), but that galaxies with compact cores have age gradients that are “more positive” (i.e., flatter) than those with diffuse cores. We have interpreted the flatter gradients as a signature of compaction, but in fact, if they are older overall, the flatter gradients could be due merely to the shorter Hubble time at their time of quenching, and not actually a relic of compaction. In other words, the difference in age between the centres and outskirts cannot be more than the Hubble time at the time of quenching. In truth, our age resolution is not sufficient to rule this out.⁸ However if we consider only quiescent galaxies with star-forming baxels (presumably those

⁷ We confirm this both using the SDSS DR7 fiber spectra as well as MaNGA spectra. Note that Fig. 6 shows that $\Delta \log \text{age}$ is lower for compact cores than for diffuse cores despite the absolute age being higher. This is because stellar age correlates strongly with Σ_* , and this dependence is removed in the computation of $\Delta \log \text{age}$ - see §2.5.

⁸ However if we adopt the age gradients of Goddard et al. (2017), these are all positive for the quiescent galaxies. We have confirmed that those with higher $\Sigma_{*,1\text{kpc}}$ have *more positive*, i.e., with steeper gradients, and this cannot be explained by the shorter Hubble time at the time of quenching.

that are quenching “now” or quenched recently), those with compact cores actually do have different profiles of sSFR and gas metallicity compared with those with diffuse cores. Thus at least today, quenching seems to retain the signatures of the two growing modes.

Our results and interpretation rely in part on the measurement of stellar ages which are notoriously difficult and prone to degeneracies and large errors (e.g., Conroy 2013). Indeed, we have found that age gradients, including their *sign*, are disturbingly inconsistent between fitting codes and different SSP templates. For example, the mass-weighted stellar age gradients computed by Goddard et al. (2017) using the Firefly fitting code and the Maraston & Strömbäck (2011) templates are strongly positive for all quiescent galaxies regardless of $\Sigma_{*,1\text{kpc}}$. Goddard et al. (2017) also cite other long-slit studies which find positive age gradients for early type galaxies. This is in contrast to the negative gradients found here, and also seen in early-type galaxies, for example, by Petty et al. (2013) (using the FSPS models of Conroy & Gunn 2010), and by Li et al. (2018) (using pPXF and the MILES models). We have found that stellar ages tend to more or less agree in the bright inner galactic regions, and that the inconsistencies seem to be in the outskirts where the S/N is lowest.

Discussing the merits and weaknesses of fitting codes and template models is beyond the scope of this work. However, when we compared the outputs of Firefly (using the Maraston & Strömbäck 2011 templates) and pPXF (using both the E-MILES and Maraston & Strömbäck (2011) templates), what we have found to be robust are the profiles of *relative* age (i.e., the difference in age of a baxel compared to other baxels of the same stellar mass density, position and global galaxy mass). If secular inside-out growth is the default growing mode of galaxies, then most age gradients should be negative (older stars in the centre). Compaction-like events would then add new stars preferentially in the centres. Regardless if such events render the overall age gradients to be positive or still slightly negative, the profiles of *relative* age (which are robust between models) should capture the effect of these dissipative events.

Furthermore, we have also presented gradients in sSFR and gas metallicities which are derived from emission line measurements. These are robust even if the underlying stellar populations that are subtracted vary between stellar population models. The disadvantage to emission line measurements is that they are not present in all areas of every galaxy since many galaxies are devoid of gas. However we have found that when present with sufficient S/N, the emission lines tell a consistent story with the relative ages.

We note that much of our discussion and interpretation has assumed that once stars are formed in situ, their positions are not significantly altered such that profiles of stellar age accurately reflect where the bulk of old and young stars were formed. The obvious events that might disturb the distribution of stars are major mergers. However, we expect that the primary effect of major mergers is to mix the orbits of pre-merger stars so as to wipe out pre-existing gradients (White 1980; Di Matteo et al. 2009). The fact that we see intact gradients which correlate with $\Sigma_{*,1\text{kpc}}$ and M_* in the way expected of dissipative compaction-like events and slower inside-out disk growth may actually attest to the lesser significance of mergers in the life of galaxies than the

events which led to their gradients. However further study is necessary to establish the effect of mergers, both major and minor, on the distribution of stellar ages, sSFR and gas metallicities in star forming and quiescent galaxies.

6 SUMMARY

We have measured the stellar ages, sSFR and gas-phase metallicities for galaxies from the SDSS DR14 MaNGA survey. By utilizing SDSS DR7 imaging data to compute the total and central stellar masses for ~ 500 of these galaxies, we studied the behaviour of the gradients and average profiles of stellar age, sSFR and O/H as a function of total mass M_* and the stellar surface density within 1 kpc $\Sigma_{*,1\text{kpc}}$. Our aim was to determine whether core-building “compaction”-like processes or progenitor effects resulting from secular disk growth are responsible for the link between quiescence and the presence of a dense stellar bulge (the morphology-quiescence relation). Our conclusions can be summarized as follows:

(i) The gradients of stellar age, sSFR and O/H for star forming galaxies depend on position in the $\Sigma_{*,1\text{kpc}}-M_*$ diagram. Galaxies on the lower part of the $\Sigma_{*,1\text{kpc}}-M_*$ relation (those with “diffuse” cores) have centres that are old, depressed in sSFR and enriched in metals. Galaxies on the upper part of the $\Sigma_{*,1\text{kpc}}-M_*$ relation (those with “compact” cores) have centres that are young, elevated in sSFR and metal-deficient compared with their outskirts (Figs. 3-5). *This is consistent with an evolutionary picture that includes both “inside-out” secular disk growth and dissipative “compaction”-like core-building processes.* The former grows galaxies along the $\Sigma_{*,1\text{kpc}}-M_*$ relation through galaxy-wide star formation. The latter brings galaxies to the upper $\Sigma_{*,1\text{kpc}}-M_*$ relation via a growth path that is steeper than the slope of the main $\Sigma_{*,1\text{kpc}}-M_*$ relation for SF galaxies.

(ii) For quiescent galaxies, the profiles of age, sSFR and O/H (when measureable) also differ between those with compact cores and those with diffuse cores (Figs. 6-8). Some residual star-forming gas is present in about 27% of quiescent galaxies. If we assume that these galaxies are those that are currently quenching or are recently quenched, then at least today, quenching retains the signatures of the two growing modes. In other words, both the inside-out growth and compaction-like growing modes contribute to the quiescent population, and the morphology-quiescence relation results from both modes.

(iii) If the quiescent galaxies represent the end point of the two evolutionary tracks, then the sSFR profiles imply that: a) galaxies that quench after the compaction-like track quench uniformly across the whole galaxy; and b) galaxies that quench after secular disk growth quench their centres first.

(iv) The WISE-selected AGN fraction peaks in the upper region of the $\Sigma_{*,1\text{kpc}}-M_*$ relation where galaxies are expected to arrive after compaction-like evolution (Fig. 9). This is consistent with compaction-like events leading to the triggering of AGN, which may be responsible for the quenching of galaxies on this track.

(v) About half of quiescent galaxies with residual star-forming gas are in the lower part of the $\Sigma_{*,1\text{kpc}}-M_*$ relation for quiescent galaxies, i.e., those that have the signatures

of the secular inside-out disk growth track. The compaction track may be more dominant at higher z while the secular mode may be increasing in importance. However, if the presence of gas indicates recent quenching, then the compaction track still continues to quench about half of recently quenched galaxies today.

From these results we conclude that star forming galaxies grow in $\Sigma_{*,1\text{kpc}}$ and M_* by both dissipative compaction-like core-building mechanisms as well as by inside-out galaxy-wide star formation, and that these two scenarios need not be mutually exclusive. Both modes seem to contribute to the morphology-quiescence relation, with varying importance over time. Compaction-like events seem to be triggered and fed by the infall of low-metallicity gas, and likely happen on top of secular disk growth, causing them to deviate from the lower track of the $\Sigma_{*,1\text{kpc}}-M_*$ diagram.

ACKNOWLEDGEMENTS

We acknowledge the helpful and stimulating discussions with Trystyn Berg, Asa Bluck, Connor Bottrell, Michele Cappellari, Avishai Dekel, Sandra Faber, Maan Hani, David Koo, Trevor Mendel, Jorge Moreno, Masato Onodera, David Patton, Luc Simard, and Mallory Thorp. SLE gratefully acknowledges the receipt of an NSERC Discovery Grant.

This research made use of Astropy,⁹ a community-developed core Python package for Astronomy (Robitaille et al. 2013; Price-Whelan et al. 2018).

This research also made use of the computation resources provided by Westgrid (www.westgrid.ca) and Compute Canada (www.computecanada.ca).

Funding for the Sloan Digital Sky Survey IV has been provided by the Alfred P. Sloan Foundation, the U.S. Department of Energy Office of Science, and the Participating Institutions. SDSS acknowledges support and resources from the Center for High-Performance Computing at the University of Utah. The SDSS web site is www.sdss.org. SDSS is managed by the Astrophysical Research Consortium for the Participating Institutions of the SDSS Collaboration including the Brazilian Participation Group, the Carnegie Institution for Science, Carnegie Mellon University, the Chilean Participation Group, the French Participation Group, Harvard-Smithsonian Center for Astrophysics, Instituto de Astrofísica de Canarias, The Johns Hopkins University, Kavli Institute for the Physics and Mathematics of the Universe (IPMU) / University of Tokyo, the Korean Participation Group, Lawrence Berkeley National Laboratory, Leibniz Institut für Astrophysik Potsdam (AIP), Max-Planck-Institut für Astronomie (MPIA Heidelberg), Max-Planck-Institut für Astrophysik (MPA Garching), Max-Planck-Institut für Extraterrestrische Physik (MPE), National Astronomical Observatories of China, New Mexico State University, New York University, University of Notre Dame, Observatorio Nacional / MCTI, The Ohio State University, Pennsylvania State University, Shanghai Astronomical Observatory, United Kingdom Participation Group, Universidad Nacional Autónoma de México, University of Arizona, University of Colorado Boulder, University of Oxford,

University of Portsmouth, University of Utah, University of Virginia, University of Washington, University of Wisconsin, Vanderbilt University, and Yale University.

REFERENCES

- Assef R. J., Stern D., Noirot G., Jun H. D., Cutri R. M., Eisenhardt P. R. M., 2018, *Astrophys. J. Suppl. Ser.*, 234, 23
- Azadi M., et al., 2017, *ApJ*, 835, 27
- Barnes J. E., Hernquist L. E., 1991, *ApJ*, 370, L65
- Baron D., et al., 2018, preprint (arXiv:1804.03150)
- Barro G., et al., 2013, *ApJ*, 765, 104
- Barro G., et al., 2017, *ApJ*, 840, 47
- Behroozi P. S., Wechsler R. H., Wu H. Y., 2013, *ApJ*, 762, 109
- Belfiore F., et al., 2018, *MNRAS*, 477, 3014
- Bell E. F., 2008, *ApJ*, 682, 355
- Bell E. F., et al., 2012, *ApJ*, 753, 167
- Blanton M. R., Roweis S., 2007, *AJ*, 133, 734
- Blanton M. R., Kazin E., Muna D., Weaver B. A., Price-Whelan A., 2011, *AJ*, 142, 31
- Blecha L., Snyder G. F., Satyapal S., Ellison S. L., 2018, *MNRAS*, 478, 3056
- Bluck A. F. L., Mendel J. T., Ellison S. L., Moreno J., Simard L., Patton D. R., Starkenburg E., 2014, *MNRAS*, 441, 599
- Bluck A. F., et al., 2016, *MNRAS*, 462, 2559
- Bournaud F., Dekel A., Teyssier R., Cacciato M., Daddi E., Juneau S., Shankar F., 2011, *ApJL*, 741, L33
- Bradford J. D., Geha M. C., Greene J. E., Reines A. E., Dickey C. M., 2018, *ApJ*, 861, 50
- Brinchmann J., Charlot S., White S. D. M., Tremonti C., Kauffmann G., Heckman T., Brinkmann J., 2004, *MNRAS*, 351, 1151
- Bundy K., et al., 2015, *ApJ*, 798, 7
- Cappellari M., 2017, *MNRAS*, 466, 798
- Cappellari M., Copin Y., 2003, *MNRAS*, 342, 345
- Cappellari M., Emsellem E., 2004, *PASP*, 116, 138
- Carollo C. M., et al., 2013, *ApJ*, 773, 112
- Cheung E., et al., 2012, *ApJ*, 760, 131
- Cheung E., et al., 2016, *Nature*, 533, 504
- Conroy C., 2013, *ARA&A*, 51, 393
- Conroy C., Gunn J. E., 2010, *ApJ*, 712, 833
- Cowley M. J., et al., 2016, *MNRAS*, 457, 629
- Cresci G., Mannucci F., Maiolino R., Marconi A., Gnerucci A., Magrini L., 2010, *Nature*, 467, 811
- Croom S. M., et al., 2012, *MNRAS*, 421, 872
- Croton D. J., et al., 2006, *MNRAS*, 365, 11
- Dekel A., Birnboim Y., 2006, *MNRAS*, 368, 2
- Dekel A., et al., 2009, *Nature*, 457, 451
- Di Matteo P., Pipino A., Lehnert M. D., Combes F., Semelin B., 2009, *A&A*, 499, 427
- Ellison S. L., Patton D. R., Mendel J. T., Scudder J. M., 2011, *MNRAS*, 418, 2043
- Ellison S. L., Mendel J. T., Patton D. R., Scudder J. M., 2013, *MNRAS*, 435, 3627
- Ellison S. L., Teimoorinia H., Rosario D. J., Mendel J. T., 2016, *MNRASL*, 458, L34
- Ellison S. L., Sánchez S. F., Ibarra-Medel H., Antonio B., Mendel J. T., Barrera-Ballesteros J., 2018, *MNRAS*, 474, 2039
- Fall S. M., Efstathiou G., 1980, *MNRAS*, 193, 189
- Fang J. J., Faber S. M., Koo D. C., Dekel A., 2013, *ApJ*, 776, 63
- Fioc M., Rocca-Volmerange B., 1999, preprint (arXiv:9912179)
- Fitzpatrick E. L., 1999, *PASP*, 111, 63
- Fluetsch A., et al., 2018, preprint (arXiv:1805.05352)
- Friedli D., Benz W., 1995, *A&A*, 301, 649
- Goddard D., et al., 2017, *MNRAS*, 466, 4731
- González Delgado R. M., et al., 2016, *A&A*, 590, A44
- Gunn J. E., Gott, J. Richard I., 1972, *ApJ*, 176, 1

⁹ <http://www.astropy.org>

- Hall C., Courteau S., Jarrett T., Cluver M., Meurer G., Carignan C., Audcent-Ross F., 2018, preprint ([arXiv:1809.09111](#))
- Ho L. C., Darling J., Greene J. E., 2008, *ApJ*, 681, 128
- Hopkins P. F., Hernquist L., Cox T. J., Di Matteo T., Robertson B., Springel V., 2006, *Astrophys. J. Suppl. Ser.*, 163, 1
- Immeli A., Samland M., Gerhard O., Westera P., 2004, *A&A*, 413, 547
- Kauffmann G., et al., 2003, *MNRAS*, 341, 33
- Kauffmann G., White S. D. M., Heckman T. M., Menard B., Brinchmann J., Charlot S., Tremonti C., Brinkmann J., 2004, *MNRAS*, 353, 713
- Kennicutt R. C., et al., 2009, *ApJ*, 703, 1672
- Kepner J. V., 1999, *ApJ*, 520, 59
- Kereš D., Katz N., Fardal M., Davé R., Weinberg D. H., 2009, *MNRAS*, 395, 160
- Kewley L. J., Groves B., Kauffmann G., Heckman T., 2006, *MNRAS*, 372, 961
- Kewley L. J., Rupke D., Jabran Zahid H., Geller M. J., Barton E. J., 2010, *ApJL*, 721, L48
- Kocevski D. D., et al., 2017, *ApJ*, 846, 112
- Kormendy J., Ho L. C., 2013, *ARA&A*, 51, 511
- Kroupa P., 2001, *MNRAS*, 322, 231
- Larson R. B., Tinsley B. M., Caldwell C. N., 1980, *ApJ*, 237, 692
- Law D. R., et al., 2016, *AJ*, 152, 83
- Lejeune T., Cuisinier F., Buser R., 1998, *Astron. Astrophys. Suppl. Ser.*, 130, 65
- Li H., et al., 2018, *MNRAS*, 476, 1765
- Lilly S. J., Carollo C. M., 2016, *ApJ*, 833, 1
- Lin L., Li C., He Y., Xiao T., Wang E., 2017, *ApJ*, 838, 105
- Liu Q., Wang E., Lin Z., Gao Y., Liu H., Teklu B. B., Kong X., 2018, *ApJ*, 857, 17
- Maraston C., Strömback G., 2011, *MNRAS*, 418, 2785
- Marino R. A., et al., 2013, *A&A*, 559, A114
- Martel H., Carles C., Robichaud F., Ellison S. L., Williamson D. J., 2018, *MNRAS*, 477, 5367
- Mateos S., Alonso-Herrero A., Carrera F. J., Blain A., Severgnini P., Caccianiga A., Ruiz A., 2013, *MNRAS*, 434, 941
- Mendel J. T., Simard L., Ellison S. L., Patton D. R., 2013, *MNRAS*, 429, 2212
- Mihos C., Hernquist L., 1996, *ApJ*, 464, 641
- Moster B. P., Naab T., White S. D. M., 2013, *MNRAS*, 428, 3121
- Nelson E. J., et al., 2012, *ApJ*, 747, L28
- Nelson E. J., et al., 2013, *ApJ*, 763, L16
- Omand C. M., Balogh M. L., Poggianti B. M., 2014, *MNRAS*, 440, 843
- Papovich C., et al., 2015, *ApJ*, 803, 26
- Peng Y. J., et al., 2010, *ApJ*, 721, 193
- Peng Y. J., Lilly S. J., Renzini A., Carollo M., 2012, *ApJ*, 757, 4
- Petty S. M., et al., 2013, *AJ*, 146, 77
- Pietrinferni A., Cassisi S., Salaris M., Castelli F., 2004, *ApJ*, 612, 168
- Price-Whelan A. M., et al., 2018, *AJ*, 156, 123
- Read J. I., Wilkinson M. I., Evans N. W., Gilmore G., Kleya J. T., 2006, *MNRAS*, 366, 429
- Ricciardelli E., Vazdekis A., Cenarro A. J., Falcón-Barroso J., 2012, *MNRAS*, 424, 172
- Robitaille T. P., et al., 2013, *A&A*, 558, A33
- Roškar R., Debattista V. P., Stinson G. S., Quinn T. R., Kaufmann T., Wadsley J., 2008, *ApJ*, 675, L65
- Salim S., et al., 2007, *Astrophys. J. Suppl. Ser.*, 173, 267
- Sánchez-Blázquez P., et al., 2014, *A&A*, 570, A6
- Sánchez S. F., et al., 2012, *A&A*, 538, A8
- Schawinski K., et al., 2014, *MNRAS*, 440, 889
- Scudder J. M., Ellison S. L., Torrey P., Patton D. R., Mendel J. T., 2012, *MNRAS*, 426, 549
- Shangguan J., Ho L. C., Xie Y., 2018, *ApJ*, 854, 158
- Simard L., Mendel J. T., Patton D. R., Ellison S. L., McConnachie A. W., 2011, *Astrophys. J. Suppl. Ser.*, 196, 11
- Strateva I., Ivezić Z., Knapp G. R., Narayanan V. K., Strauss M. A., 2001, *AJ*, 122, 1861
- Tacchella S., Dekel A., Marcella Carollo C., Ceverino D., DeGraf C., Lapiner S., Mandelker N., Primack J. R., 2016, *MNRAS*, 458, 242
- Tacchella S., Carollo C. M., Faber S. M., Cibinel A., Dekel A., Koo D. C., Renzini A., Woo J., 2017, *ApJ*, 844, L1
- Teimoorinia H., Bluck A. F., Ellison S. L., 2016, *MNRAS*, 457, 2086
- Terrazas B. A., Bell E. F., Henriques B. M. B., White S. D. M., Cattaneo A., Woo J., 2016, *ApJL*, 830, L12
- Terrazas B. A., Bell E. F., Woo J., Henriques B. M. B., 2017, *ApJ*, 844, 170
- Thorp M. D., Ellison S. L., Simard L., Sánchez S. F., Antonio B., 2018, preprint ([arXiv:1810.00897](#))
- Vazdekis A., Ricciardelli E., Cenarro A. J., Rivero-González J. G., Díaz-García L. A., Falcón-Barroso J., 2012, *MNRAS*, 424, 157
- Vazdekis A., Koleva M., Ricciardelli E., Röck B., Falcón-Barroso J., 2016, *MNRAS*, 463, 3409
- Villalobos Á., De Lucia G., Borgani S., Murante G., 2012, *MNRAS*, 424, 2401
- Wang E., Kong X., Pan Z., 2018, preprint ([arXiv:1808.05929](#))
- White S., 1980, *MNRAS*, 191, 1P
- Woo J., et al., 2013, *MNRAS*, 428, 3306
- Woo J., Dekel A., Faber S. M., Koo D. C., 2015, *MNRAS*, 448, 237
- Woo J., Carollo C. M., Faber S. M., Dekel A., Tacchella S., 2017, *MNRAS*, 464, 1077
- Woosley S. E., Weaver T. A., 1995, *Astrophys. J. Suppl. Ser.*, 101, 181
- Wuyts S., et al., 2011, *ApJ*, 742, 96
- Yang X., Mo H. J., Van Den Bosch F. C., Zhang Y., Han J., 2012, *ApJ*, 752, 41
- Zolotov A., et al., 2015, *MNRAS*, 450, 2327
- van Dokkum P. G., Franx M., 2001, *ApJ*, 553, 90
- van Dokkum P. G., et al., 2010, *ApJ*, 709, 1018
- van Dokkum P. G., et al., 2011, *ApJ*, 743, L15
- van den Bosch F. C., 1998, *ApJ*, 507, 601
- van den Bosch F. C., 2002, *MNRAS*, 331, 98

APPENDIX: THE ACCURACY OF STELLAR AGES AND METALLICITIES FROM PPIX

In order to test whether pPIX (Cappellari 2017) produces reliable estimates for stellar age and metallicity, we produced a suite of synthetic test spectra with known ages and metallicities and tested to see how well pPIX could reproduce them given the typical noise spectrum and spectral resolution of MaNGA. Our goal was to produce spectra with realistically evolving populations. Thus we chose to construct our suite of spectra out of τ -model star-formation histories with metallicities that evolved self-consistently. We used the PEGASE predictions for the evolution of the stellar metallicity of a population given the τ -models constructed in §2.2. In particular, we selected a subset of 48 of the τ -models constructed in §2.2, corresponding to initial metallicities Z of 0.004, 0.008, 0.01, 0.015, 0.02 and 0.03. Only these were selected because their metallicities evolve to values within the safe range for the use of the E-MILES SSP templates in our chosen wavelength range. Since MaNGA galaxies are all low- z massive objects we do not expect real metallicities to fall outside of this safe range.

These 48 τ -models evolve in both SFR and metallicity and this can be directly translated into evolving weights on

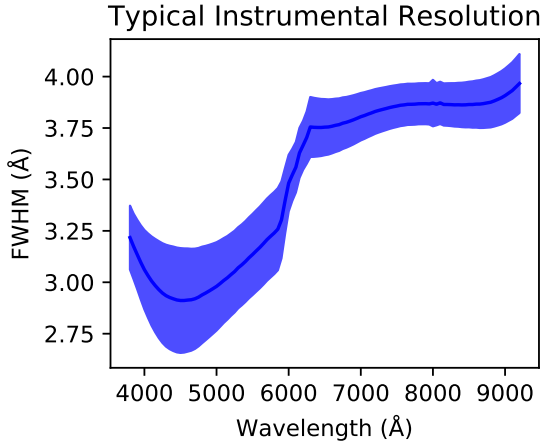


Figure A1. The median FWHM of the line spread function of MaNGA datacubes (solid line) and the standard deviation around the median (shaded region).

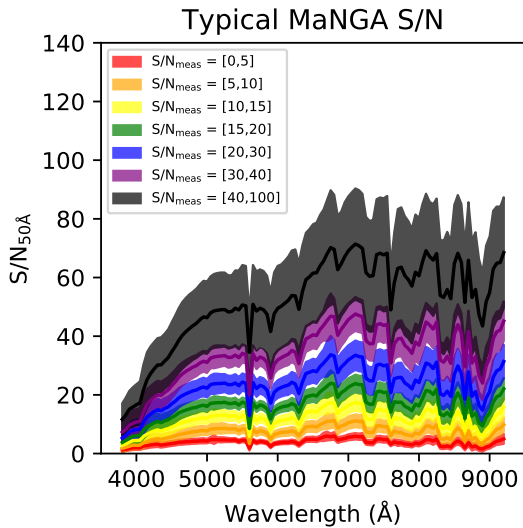


Figure A2. This plot shows the typical S/N as a function of wavelength in MaNGA baxels. $S/N_{50\text{\AA}}$ is the S/N averaged over 50 Å around the test wavelength. Each curve represents the median of all baxels within the indicated ranges of the measured S/N_{meas} , which is measured over the wavelength range of 5590–5680 Å. The shaded regions represent the standard deviation around the median.

the E-MILES age-metallicity grid of SSPs. We sample these 48 evolving models at 16 timesteps (spanning 0.05–13 Gyr) producing 768 snapshots of the weighted age-metallicity grid. A snapshot of weights can then be used to combine the spectra of the SSPs into a single spectrum for the population corresponding to a mass-weighted age and metallicity.

We also constructed a spectrum of the emission lines typical of HII regions and added them to the 768 spectra with 3 weight values (0, 5 and 10). We also added dust corresponding to 6 values of $E(B-V)$ (0, 0.15, 0.3, 0.5, 0.75, and 1.0). Up to this point we have constructed 13824 spectra,

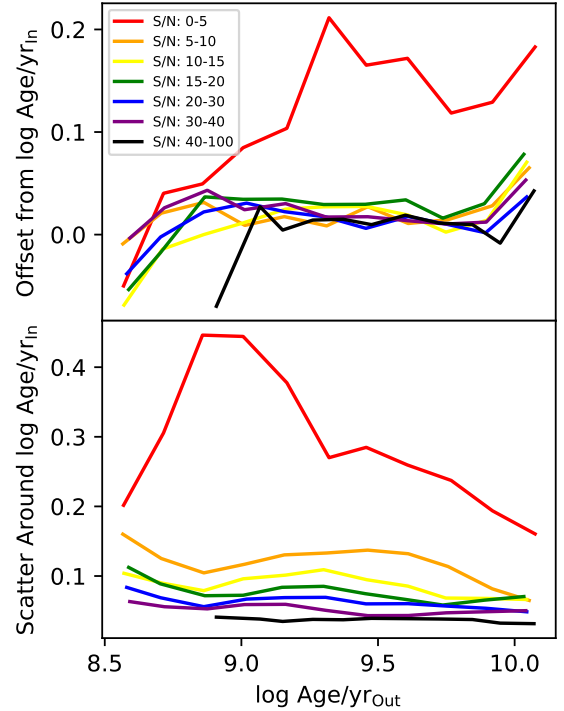


Figure A3. Top: the systematic offset between input and output ages as a function of output age and S/N. Bottom: the scatter in $\log \text{Age}_{\text{out}}/\text{yr} - \log \text{Age}_{\text{in}}/\text{yr}$.

which we convolved with the typical MaNGA instrumental spectral resolution (shown in Fig. A1).

Lastly we computed the typical noise spectrum for MaNGA baxels in 7 bins of S/N. These are shown in Fig. A2 as curves of $S/N_{50\text{\AA}}(\lambda)$, which is the S/N averaged over 50 Å around the test wavelength. The inverse of these curves is multiplied by the synthetic spectra to create noise spectra which are then added to the final spectra. Thus, we have created 96768 synthetic spectra spanning 6 initial metallicities, 8 τ values for the τ -models, 16 timesteps, 3 emission spectra, 6 reddening values and 7 typical noise spectra.

We ran pPXF on these test spectra and compared the measured mass-weighted log ages and metallicities against their input values. The following is a list of our observations from these comparisons.

- The presence and strength of emission lines has no effect on the quality of the fits.
- Dust and S/N have significant effects on the fit quality.
- Fits that are restricted to $\chi^2 < 5$ and $S/N > 10$ (93% of our MaNGA baxels) have reliable ages and metallicities. Systematic offsets and scatter were minimal and are dependent on mean S/N and output age and metallicity (see Fig. A3).
- The majority (75%) of fits with $\chi^2 > 5$ have measured $E(B-V)_{\text{stars}} > 0.28$. Dusty young populations are often mistaken for older, metal rich populations, consistent with known dust degeneracies (e.g., Conroy 2013).

Based on these tests, our science sample that involves the stellar ages include only those baxels with $\chi^2 < 5$, $S/N > 10$, $E(B-V)_{\text{stars}} < 0.28$, and $\log \text{Age}/\text{yr} > 8.5$.